Journal of Ultrafine Grained and Nanostructured Materials
https://jufgnsm.ut.ac.ir
Vol. 58, No.2, June 2025, pp. 277-286
Print ISSN: 2423-6845 Online ISSN: 2423-6837
DOI: 10.22059/jufgnsm.2025.02.12

The effect of $FeCoNiCuAl_{0.2}$ high-entropy alloy interlayer on dissimilar resistance spot welding of AISI304 to AISI420 stainless steels

Abolfazl Asgharzadeh Moalem, Mahmoud Sarkari Khorrami*

School of Metallurgy and Materials Engineering, College of Engineering, University of Tehran

Recieved: 30 August 2025; Accepted: 8 November 2025

*Corresponding author, E-mail: m.khorrami@ut.ac.ir

ABSTRACT

The widespread use of stainless steels in various industries due to their appropriate strength and corrosion resistance necessitates the investigation of dissimilar joints between them. However, resistance spot welding (RSW) of AISI304 austenitic stainless steel (ASS304) to AISI420 martensitic stainless steel (MSS420), particularly in case of employing interlayer, has not been examined so far. Due to appreciable difference in their physical properties and metallurgical consistency as main concerns, the effect of $FeCoNiCuAl_{0.2}$ high-entropy alloy (HEA) interlayer on the microstructural and mechanical behavior of the joints was investigated. It was found that copper exhibited a segregation in the HEA cast ingot because of its positive mixing enthalpy with other elements. This issue was responsible for the formation of hot cracking in the weld nugget, resulting in a decrease in mechanical strength of the joints. The effect of welding current on the joint strength was investigated as well. The relatively suitable current intensity in this joint was found to be 7 kA, and the maximum failure force was achieved in this case at about 6000 N. At lower current intensity (6 kA) due to insufficient heat input, proper fusion between the base metals and the interlayer was not formed and the maximum fracture force was about 4000 N. At 8 kA current intensity, due to higher heat input and increased weld nugget size, a higher fracture force was obtained than at 6 kA current intensity, but the displacement was reduced. The decrease in fracture toughness at 8 kA current intensity was attributed to spattering and increased copper segregation due to higher temperature (more diffusion of copper atoms).

Keywords: *Dissimilar resistance spot welding; AISI304 austenitic stainless steel; AISI420 martensitic stainless steel; Interlayer; High-entropy alloys.*

1. Introduction

Dissimilar welding of austenitic (ASS) and martensitic stainless steels (MSS) is usually used where high strength and resistance to atmospheric corrosion are required simultaneously. Dissimilar welding of metals can be used in a variety of applications where a specific combination of weld properties and cost savings are desired. Dissimilar welding can allow for versatile product design by effectively utilizing each material [1]. Austenitic stainless steels can be used in a wide range of industries due to their excellent corrosion resistance (due to a significant percentage of chromium), mechanical behavior, and biocompatibility [2]. The resistance spot welding (RSW) process for this purpose can be employed in various industries such as automotive, oil and gas, heat exchangers, and pressure vessels where the use of this type of joint can meet different needs in various working conditions, particularly corrosion resistance. One

of the challenging topics in the field of RSW is the joining of dissimilar alloys [3, 4], since consideable differences in physical properties of joint components would adversely affect the quality of weld nugget. The dissimilar joining of ASS304 and MSS420 has been challenging due to the different thermal cycling experienced by these alloys, as well as their different heat conductivity coefficients, the dissimilar joining using RSW process would face more challenges compared to other welding techniques [5]. It has been reported that the use of an interlayer in dissimilar welding can contribute to better weldability, more metallurgical consistency, and improved joint strength. For example, dissimilar RSW of AISI1008 steel and Al1100 aluminum alloy with the addition of an interlayer of graphene nanoplatelets was carried out. The application of interlayer in the form of coating on the substrates led to increased strength compared to samples without an interlayer [6]. Li et al. [7] investigated the laser welding of TiNi shape memory alloy wire to stainless steel wire using a nickel interlayer. They found that with increasing the thickness of the nickel interlayer, the joint properties improved due to the reduction of brittle intermetallic compounds (IMCs) like $TiFe_2$ and $TiCr_2$, due to the increase in nickel content in the weld. Therefore, the use of an interlayer can have a dual effect on the properties of the weld metal. Nevertheless, the use of a HEA as an interlayer can be an interesting idea in the dissimilar joining of ASS304 to the MSS420. In recent years, HEAs have emerged as a new reality in the field of advanced materials. The motivation for this innovative class of engineering materials was based on the goal of expanding the frontiers of knowledge about alloys with more than one major component. The concept can be traced back to 2004, when the first papers on the subject were published [8, 9]. Currently, a standard definition for these alloys has been proposed, in which HEAs are described as metallic compounds with at least five primary elements, with the percentage of each component varying between 5 and 35% [9]. However, other definitions include a wider range of materials, with different component amounts that can be considered [10]. HEAs exhibit a high tendency to form solid solution phases rather than IMCs because the combination of several major elements creates a high entropy of mixing [11]. HEAs also exhibit unique mechanical performance and physical properties as well as high thermal stability, which has attracted researchers' interest in the processing and use of these alloys in recent years [12]. It is expected that adding HEA filler metals or an interlayer will result in fewer IMCs, with a hard and brittle phase forming at the interface compared to welding dissimilar metals without HEA. In addition, HEAs with face-centered cubic (FCC) crystal lattice have excellent ductility, high strength and super plasticity, and good fracture toughness, which can also help improve the strength and toughness of welded joints [13]. The dissimilar laser welding of nickel-titanium shape memory alloys with ASS304 was investigated using a CoCrFeNiMn HEA interlayer. The results showed that the addition of the HEA interlayer significantly reduced the formation of brittle IMCs [14]. In another study, Azhari et al. [15] studied the microstructure and mechanical properties of dissimilar RSW between 6061-T6 aluminum alloy sheets and St-12 low-carbon steel using $Al_{0.5}$FeCoCrNi HEA interlayers of different thicknesses. Their results showed that the use of the HEA interlayer changed the type of IMCs formed from Al_xFe_y in the weld without an interlayer (direct welding) to complex IMCs and prevented cracking on the Al side of the welds. Manoochehri et al. [16] investigated the effect of CoCrCuFeNi HEA interlayer in the dissimilar friction stir welding (FSW) of AA5010 aluminum alloy to St-12 carbon steel. The HEA interlayer successfully prevented the formation of Al_xFe_y single-bonded IMCs. After investigating the mechanical properties of the joint, strengths up to 80% of the nominal strength of the aluminum base metal were achieved. In the present study, the microstructure and mechanical properties of the RSW of ASS304 to MSS420 using a $FeCoNiCuAl_{0.2}$ HEA interlayer were investigated. Also, $FeCoNiCuAl_{0.2}$ HEA interlayer were placed as thin layers between two base metals, and the RSW process was used to weld dissimilar base metals of MSS420 and ASS304 , and the effect of copper atoms segregation in the weld metal and the formation of grain boundary cracks was studied. The $FeCoNiCuAl_{0.2}$ alloy was chosen on the one hand because of its FCC structure, good mechanical performance, and on the other hand because of its innovativeness in joining using the RSW process.

2. Materials and Method

2.1. Base metal and interlayer specifications

ASS304 and MSS420 sheets with a thickness of 1.5 mm were used as starting materials. The chemical composition of the alloys, obtained from spark emission spectroscopy, as well as the mechanical properties of the base metals are listed in Tables 1 and 2, respectively. The MSS420 was in the annealed condition.

The HEA interlayer, which was produced by a vacuum arc melting (VAR) process, was cut into 500 μm thicknesses using a wire discharge cutting process. The chemical composition of the $FeCoNiCuAl_{0.2}$ HEA, obtained by energy dispersive X-ray spectroscopy analysis (EDS), is listed in Table 3 in terms of atomic percentage.

Table. 1- Chemical composition of the base metals (all in wt. %)

Alloy	Fe	C	Cr	Si	Mn	P	Co	Ni
AISI420	86.7	0.172	12.1	0.476	0.217	0.0258	0.0184	0.161
AISI304	71.7	0.0354	18	0.483	1.13	0.0326	0.283	8.11

Table. 2- Mechanical properties of the base metals [17]

Alloy	Tensile strength (MPa)	Yield strength (MPa)	% Elongation
AISI420	690	275	15
AISI304L	480	170	40

Table. 3- Chemical composition of EDS analysis of $FeCoNiCuAl_{0.2}$ HEA (all in at. %)

Element	Fe	Co	Ni	Cu	Al
Value	22.4	23.7	23.6	25.5	4.8
Nominal	23.8	23.8	23.8	23.8	4.8

2.2. RSW process and characterization

The base metal sheets were first laser-cut to a length of 100 mm and a width of 20 mm, based on the AWS D8.9M standard, which are the desired dimensions for tensile-shear mechanical testing based on the mentioned standard. To perform the welding process, the sheets were placed edge-to-edge (lap welding configuration). Before the welding process, the base metals were well cleaned of any contamination and surface oxides. Also, a HEA interlayer was used between the sheets. In this way, the interlayers were cut into small dimensions of approximately 10×10 mm^2 with a thickness of 0.5 mm and then sanded well to remove surface contaminations. A Novin Sazan Company spot welding machine, which is equipped with a cooling system under control of welding current, time, and pressure was used. The welding variables are listed in Table 4.

To investigate the microstructure of the welding samples, the cross section of samples was prepared according to standard metallography procedures followed by optical microscopy, EDS, and X-ray diffraction (XRD). The weld nuggets were electro etched using HNO_3 solution for an average time of 10 s. To investigate the phases formed, XRD was used at a scan rate of 0.05°/s in the angular range of 5° to 90° using a Cu-K irradiation. Finally, to examine the mechanical properties of the joints, a tensile-shear test was used, in which the tensile specimen dimensions were cut according to the standard, with a length of 100 mm and a width of 20 mm. Also, for better alignment of the applied tensile force, two auxiliary sheets that were roughened with coarse sandpaper were attached to the end of each specimen. To prevent the sheets from slipping, auxiliary sheets were screwed to the samples using bolts and nuts. Then, the samples were placed between the jaws of the SANTAM model machine, and the tensile test was performed at a speed of 0.5 mm/min. Also, in order to obtain the microhardness variations across the weldments, the weld nugget and the heat affected zone (HAZ), the microhardness test was performed using a Buhler machine under a load of 100 g and a dwelling time of 10 s.

3. Result and Discussion

3.1. HEA interlayer

In recent research, researchers have found that using an interlayer as a filler material in joining processes can be a good option for improving weldability, weld quality, and preventing the formation of unwanted phases, especially in dissimilar joints. According to recent results from the research of Wang et al. [14], Zhou et al. [18], and Azhari-Saray et al. [15], melting of the interlayer between the base metals and proper mixing of the molten interlayer with the base metals, and ultimately the formation of a proper metallurgical bond at the interface of the base metals and the interlayer is considered one of the important factors for achieving high mechanical properties. Therefore, the interlayer should have a melting point close to or lower than the base metals and also form a solid solution with the base metals.

3.2. Design and characterization of HEA $FeCoNiCuAl_{0.2}$

In past research, the elements iron, cobalt, chromium, nickel, copper, and aluminum have generally been used to produce HEAs for use as an interlayer [15, 18]. In another research, Du et al. [19] employed an interlayer of the high-entropy, refractory alloy TiAlNbHf to improve welding quality. However, the high cost of these elements confined their use for common applications. The enthalpy of binary fusion of the elements used in the interlayer is listed in Table 5 [20].

According to the data on binary enthalpy and applying thermodynamic calculations [20], the value of the enthalpy of fusion for the $FeCoNiCuAl_{0.2}$ HEA was calculated to be 875 J/mol. Also, the entropy of mixing was calculated according to the thermodynamic relationship of configuration entropy of mixing [21], 12.2 J/molK. Based on this calculation, the alloy falls within the range of HEAs. Hence, the formation of a solid solution and the absence of brittle IMCs were possible. Also, according to thermodynamic relations [22], the melting temperature of this alloy was found to be about 1631 K. Figure 1 shows the optical microstructure of the $FeCoNiCuAl_{0.2}$ alloy under different magnifications. As can be seen in the image, the microstructure consists of a dendritic structure resulting from the vacuum casting process. Dark regions are visible among the dendritic phase, attributed to the segregation of Cu-rich phase caused by its positive mixing entropy with other elements.

The XRD pattern of the $FeCoNiCuAl_{0.2}$ alloy are shown in Figure 2. As it is clear, the crystal structure in this alloy is a single-phase FCC crystal structure, and no trace of the formation of brittle phases was observed. The small overlap observed in the first peak can be attributed to the segregation of copper atoms. The diffraction of crystal planes occurred in the same family planes (111), (200), and (220), which is in agreement with the results of other researchers [23] and indicated the existence of a single-phase FCC structure.

Table. 4- Various welding parameters

Welding current (kA)	Electrodes force (bar)	Welding time (s)	Overlap length (mm)
6, 7, 8	3	0.1	3

Table. 5- Enthalpy of binary fusion (in kJ/mol) of elements present in the interlayer [20]

Element	Fe	Co	Ni	Cu	Al
Fe	0	-1	-2	13	-11
Co	-1	0	0	6	-19
Ni	-2	0	0	4	-22
Cu	13	6	4	0	-1
Al	-11	-19	-22	-1	0

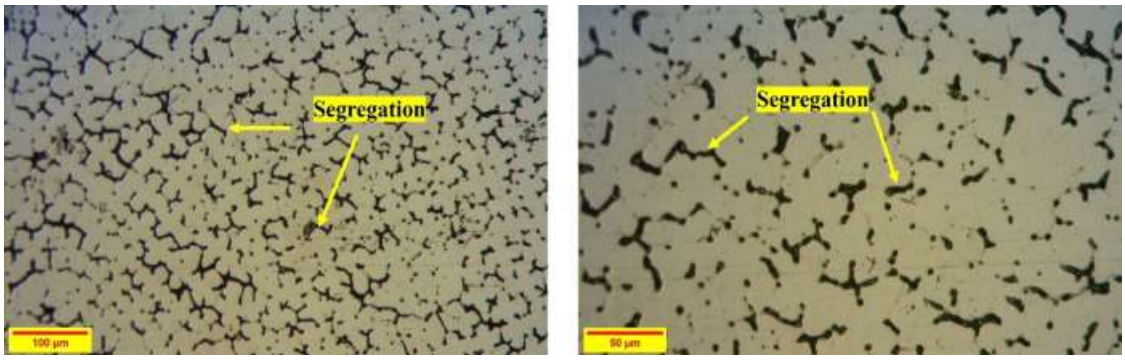

Fig. 1- Optical microscope image of the $FeCoNiCuAl_{0.2}$ HEA produced by VAR process.

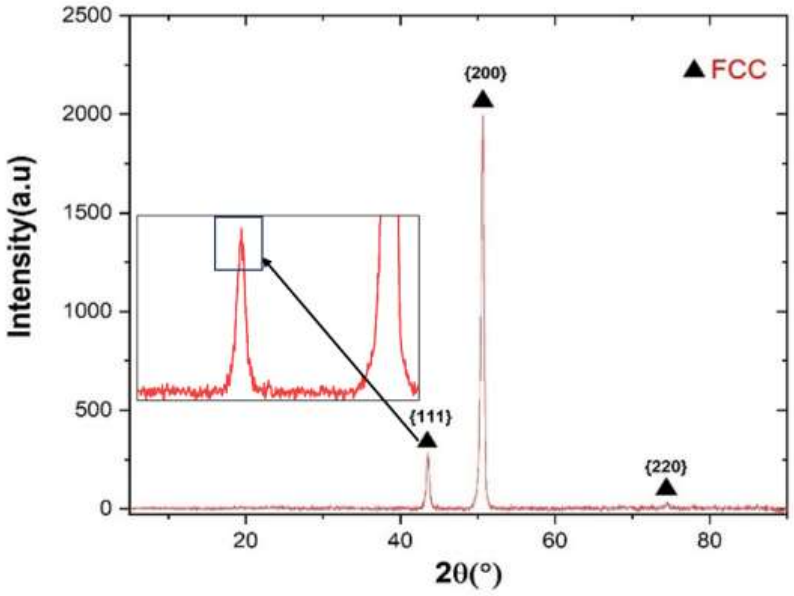

Fig. 2- XRD pattern for the $FeCoNiCuAl_{0.2}$ HEA.

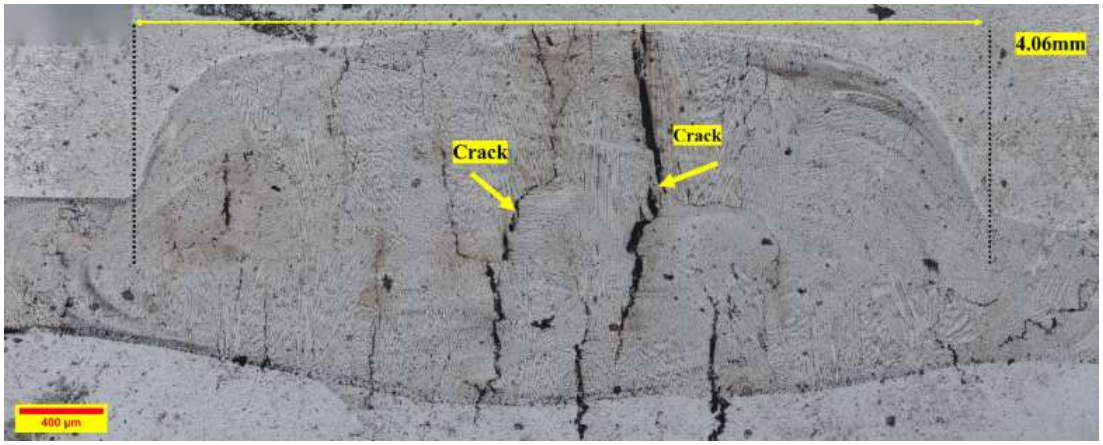

Fig. 3- Weld nugget in a dissimilar joint of MSS420 to ASS304 using a HEA interlayer and welding current of 7 kA.

3.3. Welding using a HEA interlayer

Figure 3 shows an enlarged image of the weld nugget in the dissimilar joint at the 7kA current intensity. As shown, many cracks were observed in the weld structure. The length of these cracks was calculated using Image J software, and the average crack length of the weld nugget was measured to be 825 μm. The weld nugget diameter was also measured to be 4 mm. The joint formed under an electric current intensity of 7 kA was considered as the better joint due to its higher failure force than the other samples (as will be explained in the mechanical properties section). The displacement to failure rate for this sample was also higher than for the other joints. This is while in general, in spot welding, the failure force increases with increasing current intensity and, consequently, the diameter of the welding nugget. However, in the joint with a current intensity of 7 kA, a higher failure force was achieved than in the case of 8 kA.

Higher magnification optical microscope images are shown in Figure 4. According to Figure 4a, the microstructure of the weld nugget consists of equiaxed and columnar dendrites. Figure 4b shows the cellular structure formed in the weld nugget for the joint under a current intensity of 7 kA. This was attributed to the thermal gradient (G_L) and cooling rate(R) in the weld nugget. In general, due to the high G_L in the central areas of the weld pool and the low R (due to heat released from the adjacent areas), it can be expected that the G_L/R fraction increased. An increase in the G_L/R fraction can lead to the formation of cellular structures. As shown in Figure 4c, cracks are mainly formed along grain boundaries, which can be attributed to the segregation of copper at the grain boundaries. Due to the increase in temperature and the increase in the diffusion coefficient as a result of the increase in temperature, segregation of copper atoms at the grain boundaries can occur, and copper atoms accumulate at the grain boundaries. Due to the lower melting and freezing point of copper (1085°C) compared to the other elements in the weld nugget (except aluminum, which is less than five percent), the segregated copper atoms freeze more slowly, and in this case, grain boundary melting occurs. The grain boundaries suffer a loss of strength. During solidification, grains exert compressive stress due to shrinkage on grain boundaries, and grain boundaries are subject to tensile stresses. Due to the poor mechanical properties of grain boundaries and insufficient strength to withstand tensile stress, cracks occur at grain boundaries during solidification. For this reason, grain boundaries can be prone to cracking.

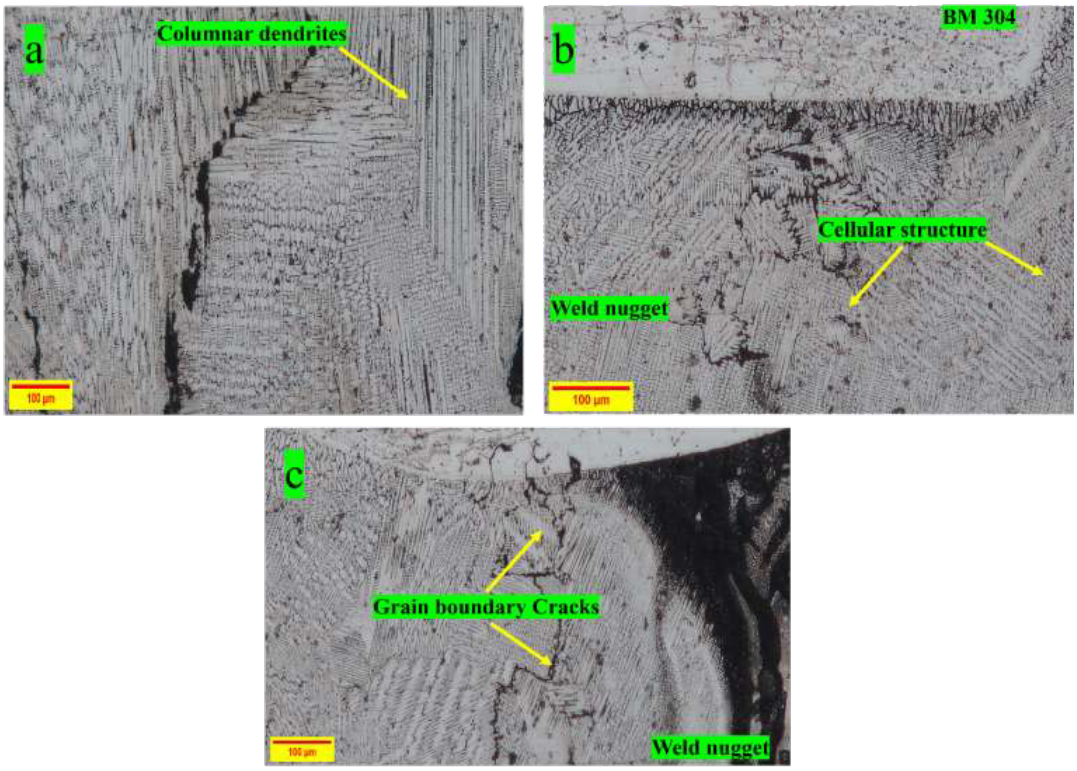

Fig. 4- Microstructure image of the weld nugget: a) Columnar dendrites, b) Cellular structure, c) Grain boundary cracks in the weld nugget due to excessive segregation of copper atoms. Welding current is 7 kA.

Figure 5a shows the microstructure of the HAZ on the MSS 420 side of the joint under a current intensity of 7 kA. A large volume fraction of precipitations exists in the HAZ, which was attributed to the chromium carbide formation. The high cooling rate during RSW process prohibited the dissolution of these phases.

Figure 5b shows the cellular structures and columnar dendrites in the center of the weld nugget for the joint formed under a current intensity of 7 kA. As discussed earlier, G_L and R in the weld pool can be considered as two important factors in the stable solidification structure. The G_L/R fraction can be considered as a controlling factor of the solidification microstructure. In the center of the weld nugget, due to the high G_L and the lower R compared to the interface areas of the base metals and the weld nugget, it can lead to an increase in the G_L/R fraction. Therefore, the morphology of columnar dendrites and cellular structures was attributed to the increase in the G_L/R fraction.

Figure 6a shows the optical microscope image of the weld nugget under 6 kA current intensity. As can be seen in the image, a proper and symmetrical weld nugget was not formed due to the low heat input. The lack of heat input on the one hand and the heat absorption by the HEA interlayer on the other hand resulted in a small weld nugget. Although the heat input was lower in this case than the current intensity of 7 kA, cracks due to copper segregation were observed in the weld nugget. However, due to the lower heat input and the reduced migration of copper elements to the grain boundaries, the number of cracks decreased compared to the current intensity of 7 kA, and the average crack length was measured to be about 260 µm. As shown in Figure 6b, the solidification structure in this joint consisted of cells. This was attributed to the thermal gradient at lower current intensity. Figure 6c shows a higher magnification image of cellular structure.

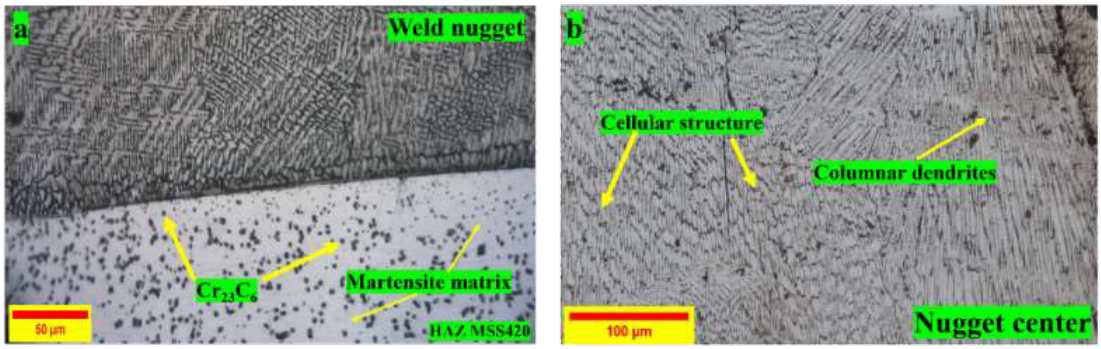

Fig. 5- a) HAZ on the MSS 420 side, b) solidification structures in the center of the weld nugget. Welding current is 7 kA.

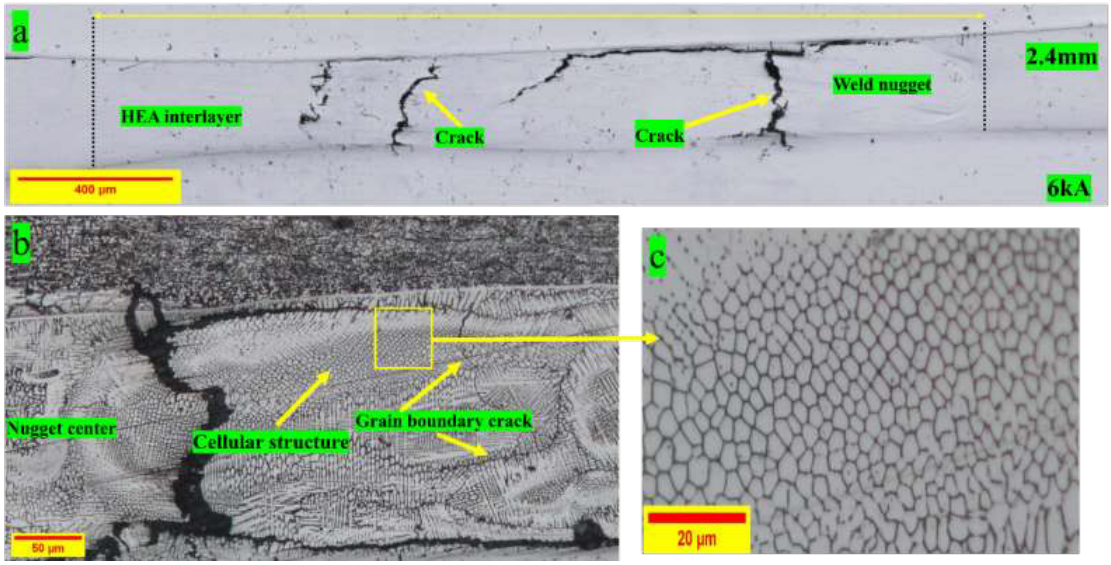

Fig. 6- Joint under 6 kA current intensity: (a) macrostructure image of the weld nugget, (b) microstructure of the weld nugget, and (c) cellular structure as the dominant microstructure.

3.4. Investigation of mechanical properties

Finally, after examining the welded structures, the mechanical properties of the joints, including the tensile-shear test and microhardness test results, were investigated. The tensile-shear test was obtained for the welded samples under different currents, and the results were compared with each other. Figure 7a shows the results of the tensile-shear test in the joint. As explained in the previous sections, microcracks due to copper segregation were observed at lower forces, and the fractures were of the interfacial (IF) type. In the IF mode, the failure occurs at the interface between the welded sheets. In contrast, in the pullout (PO) failure mode, the failure involves the weld nugget being peeled off while at least part of the weld nugget remains attached to one of the metal sheets [24]. In the current study, all joints fractured at the interface of HEA interlayer and the MSS420 base metal. The highest force among these joints was related to the connection under an electric current of 7 kA. Then, after that, due to the greater accumulation of segregation elements, the high increase in heat input, and the formation of numerous microcracks and the creation of an undesirable weld structure, the failure force gradually decreased. At the current intensity of 6 kA, the failure force was lower than that at the current intensity of 7 kA due to the lack of proper mixing of the base metals with the interlayer (due to low heat input). At the current intensity of 8 kA, the failure force was higher than that at the current intensity of 6 kA due to the increase in temperature and the increase in the size of the weld nugget, but due to excessive heat input and severe molten spattering, the failure force and displacement to failure were lower than that at the current intensity of 7 kA.

The results of the microhardness test are shown in Fig. 7b. For the connection at a current of 6 kA, the microhardness in the HAZ on the MSS420 side was higher than that of the other samples. In general, three important factors can be effective in the dissolution of chromium carbide precipitates, including cooling rate, heating rate, and heating time. In this joint, due to the relatively low heat input compared to the currents of 7 and 8 kA, in the weld nugget at the current of 6 kA, sufficient mixing between the interlayer and the base metals, especially with MSS420, was not achieved. Therefore, this can lead to an increase in the heating rate during the formation of the weld nugget. With an increase in the heating rate, the dissolution temperature of chromium carbide deposits increased. Due to the higher cooling rate when using the HEA interlayer (due to insufficient mixing with the base metals and the low height of the weld nugget, and the greater role of the base metals during cooling), sufficient time was not provided for the dissolution of chromium carbide deposits. These deposits remained continuously in the field. Therefore, the high microhardness in the HAZ on the MSS420 side compared to the samples welded under currents of 7 and 8kA when using a HEA interlayer can be attributed to the continuous precipitation of chromium carbides in the matrix and the lack of dissolution of these deposits. Also, the microhardness in the weld nugget showed a lower value and was measured at about 130HV to 180HV; these results were almost the same as those observed in the studies of Wang et al. [23]. The low microhardness in this area was attributed to the formation of a soft FCC matrix. The microhardness in the weld nugget was higher than that of the $FeCoNiCuAl_{0.2}$ cast alloy, which was attributed to

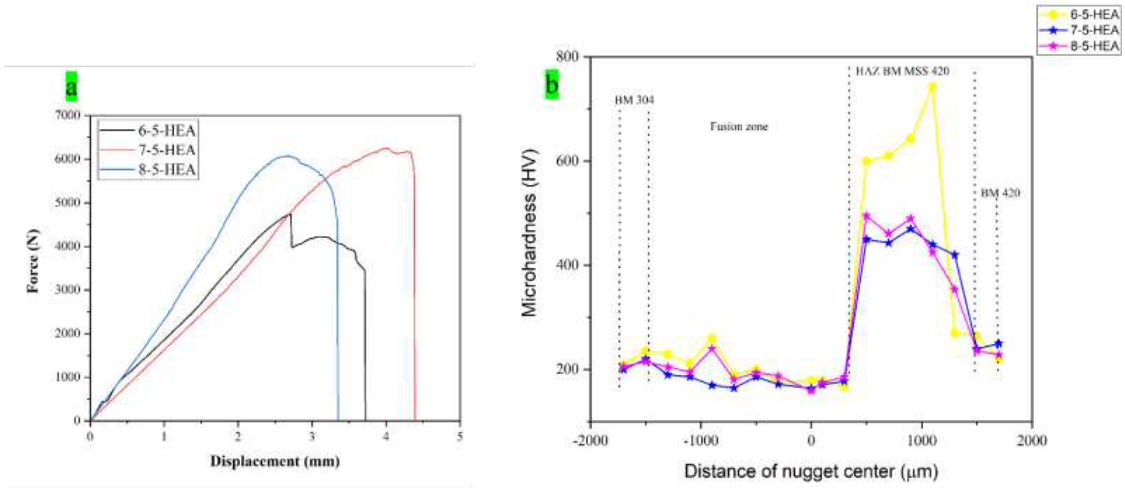

Fig. 7- (a) Force-displacement diagrams obtained from tensile-shear test and (b) microhardness profiles for joints fabricated by a HEA interlayer and various current intensities of 6, 7, and 8 kA and welding cycles of 5.

the high cooling rate in the RSW process, the finer dendrites, and the increase in equiaxed dendrites in the matrix. The microhardness in the HAZ was lower on the ASS304 side than on the weld nugget. This decrease in microhardness was attributed to the larger austenitic grains on the ASS side. With increasing electric current intensity, due to the increase in the size of the weld nugget and the greater mixing of the base metals with the interlayer, it can be expected that the heating rate and the dissolution temperature of chromium carbides in this case will decrease. On the other hand, due to the increase in the size of the weld nugget, the cooling rate decreased. Therefore, sufficient opportunity was provided for the dissolution of chromium carbide precipitates on the MSS420 side, and the microhardness in this area was lower at currents of 7 and 8 kA than at currents of 6 kA.

4. Conclusion

In this research, RSW between ASS304 and MSS420 was performed using a HEA interlayer in the electric current values of 6, 7, and 8 kA with a constant welding time of 0.1 s and a constant electrode pressure of 3 bar. The results of this research can be summarized as follows:

1. In this connection, due to the severe segregation of copper at the grain boundary and the formation of IMCs due to the presence of copper and aluminum elements with base metal elements, a suitable weld nugget was not achieved. The failure mode in these connections was entirely IF mode, and the maximum failure force was about 6000 N.

2. The microhardness for all welds in the HAZ was maximum on the MSS420 side. This result was attributed to the presence of martensite phase and the formation of continuous chromium carbide precipitates in the HAZ of the MSS420 side. Also, the microhardness in the HAZ on the ASS304 side decreased, which was due to the growth of austenite grains resulting from increased heat input.

3. The use of an interlayer increased the required electrical current. This was attributed to the heat absorption by the interlayer and the increase in the heat input required for melting and forming a suitable weld nugget.

5. future works

Further examinations may include the design of a HEA interlayer in which the segregation of low-melting phase is not concerned. Other issues may include the simulation of welding process using the finite element method to predict the diameter of the weld nugget and achieve optimal parameters without the trial-and-error, employing CALPHAD phase diagrams to design HEAs, examining the change in the thickness of the interlayer as a fundamental variable, and designing a copper-free HEA interlayer to eliminate hot cracking phenomenon.

References

1. A. Malekan, M. Malekan, N. Banimostafa Arab, and H. Bayat Tork, "Microstructure and mechanical properties in dissimilar friction stir welding of 316 stainless steel to 4140 steel," Journal of Ultrafine Grained and Nanostructured Materials, vol. 56, no. 2, pp. 147-156, 2023.
2. S. Mohammadzehi and H. Mirzadeh, "Grain refinement of austenitic stainless steels by cross rolling and annealing treatment: A review," Journal of Ultrafine Grained and Nanostructured Materials, vol. 57, no. 2, pp. 112-119, 2024.
3. R. Kacar and O. Baylan, "An investigation of microstructure/property relationships in dissimilar welds between martensitic and austenitic stainless steels," Materials & Design, vol. 25, no. 4, pp. 317-329, 2004.
4. Z. Sun and H.-Y. Han, "Weldability and properties of martensitic/austenitic stainless steel joints," Materials science and technology, vol. 10, no. 9, pp. 823-829, 1994.
5. S. S. Sashank, S. Rajakumar, and R. Karthikeyan, "Dissimilar welding of austenitic and martensitic stainless steel joints for nuclear applications: a review," in E3S Web of Conferences, 2021, vol. 309: EDP Sciences, p. 01187.
6. T. Das, R. Das, and J. Paul, "Resistance spot welding of dissimilar AISI-1008 steel/Al-1100 alloy lap joints with a graphene interlayer," Journal of Manufacturing Processes, vol. 53, pp. 260-274, 2020.
7. H. Li, D. Sun, X. Cai, P. Dong, and W. Wang, "Laser welding of TiNi shape memory alloy and stainless steel using Ni interlayer," Materials & Design, vol. 39, pp. 285-293, 2012.
8. B. Cantor, I. T. Chang, P. Knight, and A. Vincent, "Microstructural development in equiatomic multicomponent alloys," Materials Science and Engineering: A, vol. 375, pp. 213-218, 2004.
9. J. W. Yeh et al., "Nanostructured high-entropy alloys with multiple principal elements: novel alloy design concepts and outcomes," Advanced engineering materials, vol. 6, no. 5, pp. 299-303, 2004.
10. D. B. Miracle and O. N. Senkov, "A critical review of high entropy alloys and related concepts," Acta Materialia, vol. 122, pp. 448-511, 2017.
11. B. Choi et al., "Achievement of superior strength in Al–Ni dissimilar joints through designing high-entropy alloy interlayer and post weld heat treatment," Journal of Materials Research and Technology, 2025.
12. S. Daryoush, H. Mirzadeh, and A. Ataie, "Nanostructured high-entropy alloys by mechanical alloying: A review of principles and magnetic properties," Journal of Ultrafine Grained and Nanostructured Materials, vol. 54, no. 1, pp. 112-120, 2021.
13. Z. Kang, Y. Wenxiao, R. Baokai, W. Gang, and Y. Ping, "Microstructure and mechanical properties of resistance spot welded dissimilar aluminum/steel joints fabricated using high entropy alloy as interlayer," Materials Characterization, vol. 216, p. 114278, 2024.
14. H. Wang, J. Xie, Y. Chen, W. Liu, and W. Zhong, "Effect of CoCrFeNiMn high entropy alloy interlayer on microstructure and mechanical properties of laser-welded NiTi/304 SS joint," Journal of materials research and technology, vol. 18, pp. 1028-1037, 2022.
15. H. Azhari-Saray, M. Sarkari-Khorrami, A. Nademi-Babahadi, and S. F. Kashani-Bozorg, "Dissimilar resistance spot welding of 6061-T6 aluminum alloy/St-12 carbon steel using a high entropy alloy interlayer," Intermetallics, vol. 124, p. 106876, 2020.
16. S. Manoochehri and M. S. Khorrami, "Friction stir welding of AA5010 aluminum alloy to St-12 carbon steel using CoCrCuFeNi high entropy alloy interlayer," Journal of Manufacturing Processes, vol. 99, pp. 298-309, 2023.

17. J. C. Lippold and D. J. Kotecki, Welding metallurgy and weldability of stainless steels. 2005.
18. H. Zhou, X. Gu, X. Gu, J. Dong, and G. Xu, "Improvement in microstructure and mechanical properties of laser welded steel/aluminum alloy lap joints using high-entropy alloy interlayer," Journal of Materials Research and Technology, vol. 20, pp. 139-146, 2022.
19. Y. Du et al., "Microstructure and mechanical properties of Ti2AlNb diffusion bonding using multi-phase refractory high-entropy alloy interlayer," Materials Science and Engineering: A, vol. 836, p. 142688, 2022.
20. A. Takeuchi and A. Inoue, "Classification of bulk metallic glasses by atomic size difference, heat of mixing and period of constituent elements and its application to characterization of the main alloying element," Materials transactions, vol. 46, no. 12, pp. 2817-2829, 2005.
21. C. Zhang, F. Zhang, S. Chen, and W. Cao, "Computational thermodynamics aided high-entropy alloy design," Jom, vol. 64, no. 7, pp. 839-845, 2012.
22. A. Mirshekari, G. R. Khayati, and S. Arjmand, "TIG-clad Fe-based AlCoCrNiTi0. 5 high-entropy alloy coating on low-carbon steel: microstructure, microhardness, and corrosion resistance," Surface and Coatings Technology, p. 132826, 2025.
23. W.-R. Wang, W.-L. Wang, S.-C. Wang, Y.-C. Tsai, C.-H. Lai, and J.-W. Yeh, "Effects of Al addition on the microstructure and mechanical property of AlxCoCrFeNi high-entropy alloys," Intermetallics, vol. 26, pp. 44-51, 2012.
24. C. Qian, H. Ghassemi-Armaki, L. Shi, J. Kang, A. S. Haselhuhn, and B. E. Carlson, "Competing fracture modes in Al-steel resistance spot welded structures: Experimental evaluation and numerical prediction," International Journal of Impact Engineering, vol. 185, p. 104838, 2024.